Comparative Evaluation of Polyphase Bearingless Slice Motors for Fluid-Handling Applications

Martin T. Bartholet, *Member, IEEE*, Thomas Nussbaumer, *Member, IEEE*, Siegfried Silber, *Member, IEEE*, and Johann W. Kolar, *Senior Member, IEEE*

***Abstract*—For the bearingless slice motor (BSM) concept, which has been successfully introduced in semiconductor fluid-handling and medical applications over the last years, different motor configurations in terms of stator construction, number of phases, and winding arrangement exist. This paper comparatively evaluates these topologies for their suitability in possible future industry applications, such as the food, biotechnology, and pharmaceutical industries. The comparison is carried out for two-, three-, and four-phase BSM concepts based on performance indexes such as motor losses, losses in the power electronics, and voltampere requirements depending on the required magnetic bearing force and the motor torque. Finally, the performance data are discussed, and also, practical aspects such as realization effort, copper and iron mass, control effort, and scalability of the concepts are taken into account.**

***Index Terms*—Bearingless motors, fluid handling, losses, magnetic levitation, motor torque.**

I. Introduction

In TODAY'S bearingless pump systems, which have successfully been launched on the market, a two-phase bearingless motor with a symmetrical configuration of the drive and bearing windings is used to actively control the impeller of the pump. This pump setup offers several advantages compared with conventional pumps currently employed in semiconductor and medical applications. The various benefits for the handling of ultrapure and aggressive fluids in these markets are described in literature [1], [2]. A schematic cut view of the motor in its compact temple motor configuration is shown in Fig. 1. Therefore, it is shown that the stabilization of the impeller of the pump is realized with contactless magnetic bearings that are placed around the claws, which are carrying the flux of the bearing and drive system. The six spatial degrees of freedom of the rotor are stabilized magnetically through the housing wall. For the bearingless slice motor (BSM) concept, this is done passively for three of them, i.e., the axial displacement (in z-direction) and the angular displacement (tilting in x- and y-directions). The three remaining degrees of freedom are controlled actively, i.e., the radial displacement (in x- and y-directions) and the rotation of the rotor. Therefore, the active motor part generates the drive torque as well as the radial magnetic bearing forces.

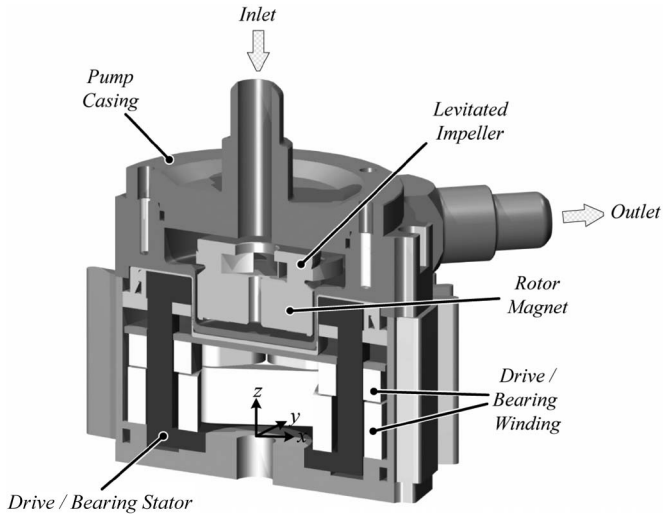

Fig. 1. Schematic of the basic principle of a centrifugal pump based on the BSM concept.

Due to the fact that the design of a bearingless motor offers a lot of constructive freedom, several different topologies have been developed over the last years [3]–[9]. They often highly differ in the way how the bearing forces and the motor torque are generated. When looking at the winding configuration, they can be broadly categorized into two groups. First, they can be categorized into those which are comprised of a dual set of winding configurations [3]–[6] where the drive and bearing windings are arranged separately (similar to the configuration shown in Fig. 1) and spread over one or more claws. The second group comprises configurations, which only have a single set of windings that carry both the torque and the levitation currents [7]–[9]. Furthermore, the proposed setups are different in terms of the number of phases for the drive and the bearing system, such as two-, three-, and four-phase systems.

To this day, only the pump concept shown in Fig. 1 and described in [2] has been employed in industry applications, such as blood pumps as heart assistance devices [10] and

Paper 2008-EMC-030.R1, presented at the 2007 International Conference on Power Electronics and Drives Systems, Bangkok, Thailand, November 27–30, and approved for publication in the IEEE TRANSACTIONS ON INDUSTRY APPLICATIONS by the Electric Machines Committee of the IEEE Industry Applications Society. Manuscript submitted for review June 25, 2008 and released for publication March 23, 2009. First published July 14, 2009; current version published September 18, 2009.

M. T. Bartholet is with Celeroton AG, 8092 Zurich, Switzerland (e-mail: martin.bartholet@celeroton.com).

T. Nussbaumer is with Levitronix GmbH, 8005 Zurich, Switzerland (e-mail: nussbaumer@levitronix.com).

S. Silber is with Johannes Kepler University Linz, 4040 Linz, Austria, and also with the Linz Center of Mechatronics GmbH, 4040 Linz, Austria (e-mail: siegfried.silber@jku.at).

J. W. Kolar is with the Power Electronic Systems Laboratory, Swiss Federal Institute of Technology (ETH) Zurich, 8092 Zurich, Switzerland (e-mail: kolar@lem.ee.ethz.ch).

Digital Object Identifier 10.1109/TIA.2009.2027366

ultrapure fluid pumps in the semiconductor industry [1]. However, for new markets, where the employment of bearingless pumps could also be highly interesting, probably, different motor concepts in terms of winding configuration and number of phases could be advantageous. Therefore, in this paper, a comparative evaluation of some selected promising polyphase BSM configurations is performed, which can serve as a calculation and selection guideline for development engineers.

The potential markets for a next-generation bearingless pump system are shown in Fig. 2. Pharmaceutical, biotechnology, and food-processing applications do also require a very high level of purity in the fluid-handling process. They demand a high degree of sterility and precision to ensure the quality of the end product, e.g., drugs, enzymes in biochemical processes or dairy, and cereal and beverages in food-processing applications. Standard centrifugal pumps cannot be used in these applications, since their ceramic housing does not sustain the hot steam, which is commonly used to sterilize the process plant. Therefore, mainly tube pumps are used in these applications. Contrary to centrifugal pumps, tube pumps have a much shorter service and maintenance interval which diminishes their acceptance in these markets and underlines the necessity for an evaluation of alternative pump concepts suitable for fluid-handling applications in general with a lower complexity than that of today's commercially available bearingless pump systems. Aside from this area, a big potential for such systems is also located in applications where magnetically coupled pumps are currently used to deliver hazardous materials, e.g., chromic acid, sodium hypochlorite, or sulfur dioxide. The biggest advantage of a bearingless pump compared with magnetically coupled pumps lies in the fact that they can run dry without the destruction of their bearings and thus offer an extended lifetime in comparison to standard magnetically coupled pumps. Another very attractive market is the plating market. The problem with magnetically coupled pumps in that area is that the plating material tends to be deposited in the narrow bearing gap. This can potentially result in a locking of the bearing. This problem particularly arises in copper-, gold-, and nickel-plating processes and often leads to down times of the production plant and subsequently large maintenance costs of the pumps. Again, both factors can be significantly reduced with the use of a bearingless pump. Additional potential markets for BSM pumps with a strong demand for long durability without maintenance are heating and cooling pumps.

For a comprehensive comparison, the motor performance of each configuration is evaluated based on performance indexes regarding power electronic requirements, the motor losses (including copper and iron losses), and the power electronic losses depending on the chosen pump operating point and the necessary bearing forces. First, the mathematical background for the calculation of the performance parameters is presented in Section II. Starting with the characteristics of the two-phase BSM with separated bearing and drive systems for torque and force generation, four additional polyphase BSM configurations are presented and explained in Section III. The evaluation of these concepts is subsequently carried out in Section IV, where a detailed comparison of the copper, the iron, and the power electronic losses occurring in the different embodiments

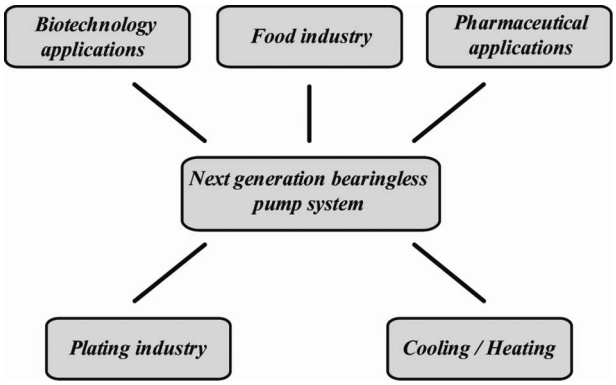

Fig. 2. Future application areas of bearingless pump systems.

is presented. Furthermore, in Section V, the necessary power electronic voltampere (VA) requirements needed to guarantee the required performance of each motor is calculated. Finally, in Section VI, cost-related realization issues are discussed for the different concepts, and the suitability of the presented assemblies for future applications of bearingless pump systems is evaluated.

II. Force and Torque Calculation

In a bearingless motor, two magnetic force types may contribute to a resulting bearing and/or drive force, namely, the Lorentz and the Maxwell forces. With the analytical force and torque model, which was first presented in [11] for the design of BSMs in disk shape with concentrated coils, these quantities can be evaluated. The model is valid under the assumption of a completely linear system where the impeller, meaning the rotor of the motor, is positioned exactly in the center of the iron circuit and no unbalances are present. Furthermore, no saturation of the iron circuit is occurring, and any armature reaction is neglected. In the following, only a brief summary of the theoretical fundamentals will be given here. Continuative information on the analytical model can also be found in [12].

With the precise knowledge of the electromagnetic field variables in the air gap (which have to be derived, e.g., by electromagnetic 3-D simulations), a general force and torque model can be derived with the use of the Maxwell stress tensor $\mathbf{T}_M$ [13]

$$\mathbf{T}_M = \mu \begin{bmatrix} H_t^2 - \frac{1}{2}H^2 & H_t H_n & H_t H_z \\ H_n H_t & H_n^2 - \frac{1}{2}H^2 & H_n H_z \\ H_z H_t & H_z H_n & H_z^2 - \frac{1}{2}H^2 \end{bmatrix}. \quad (1)$$

Here, H is the magnetic field intensity, which is composed of

$$\mathbf{H} = [\, H_t \quad H_n \quad H_z \,]^{\mathrm{T}}, \qquad H = |\mathbf{H}| \quad (2)$$

and μ is the permeability. The mechanical stress $\boldsymbol{\sigma}$ acting on a surface element can then be calculated with

$$\boldsymbol{\sigma} = \mathbf{T}_M \mathbf{e}_n \quad (3)$$

where $\mathbf{e}_n$ represents the vector perpendicularly to the stator surface (cf. Fig. 3). Furthermore, it is assumed that the permeability of the ferromagnetic stator is much higher than that of

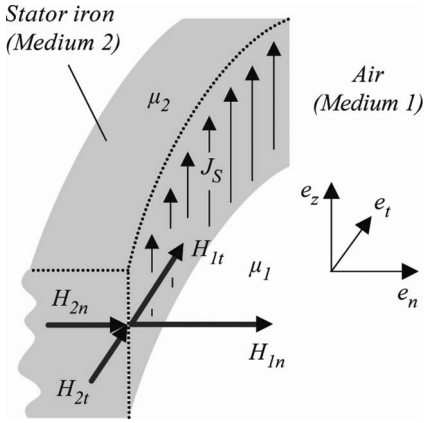

Fig. 3. Stator surface with current density distribution and field strength in the air gap.

air ($\mu_2 \gg \mu_1$), and thus, the tangential component of the flux density H_{1t} in the air gap can be neglected for the following calculation of the torque and the forces responsible for the levitation of the impeller.

With this, the mechanical tension $\boldsymbol{\sigma}_{12}$ on the interface between air (medium 1) and stator iron (medium 2) can be approximated by

$$\boldsymbol{\sigma}_{12} = \begin{bmatrix} \frac{\boldsymbol{B}_{1n}^2}{2\mu_0} \\ \boldsymbol{B}_{1n}\boldsymbol{J}_s \\ 0 \end{bmatrix} \tag{4}$$

where J_s is the current density distribution on the stator surface, which is assumed to be of cylindrical shape, and B_{1n} is the normal component of the flux density in air. Furthermore, $B_{1n}^2/2\mu_0$ represents the Maxwell force, and $B_{1n}J_s$ the Lorentz force.

The forces acting on the rotor of the BSM are then determined by the surface integral

$$\mathbf{F} = \oint_A \boldsymbol{\sigma}_{12} dA \tag{5}$$

where A represents the area of the surface. With the help of (5), the torque M_s (depending on the rotor angle α) and the force $\mathbf{F}_s$ which act on the rotor can be calculated as

$$M_s = -\, l_s r_s^2 \int_{-\pi}^{\pi} B_{1n} A_s d\alpha \tag{6}$$

$$\mathbf{F}_s = -\, l_s r_s \int_{-\pi}^{\pi} \begin{bmatrix} \cos\alpha & -\sin\alpha & 0 \\ \sin\alpha & \cos\alpha & 0 \\ 0 & 0 & 1 \end{bmatrix} \cdot \begin{bmatrix} \frac{B_{1n}^2}{2\mu_0} \\ B_{1n} A_s \\ 0 \end{bmatrix} d\alpha. \tag{7}$$

Here, l_s represents the length of the stator, and r_s represents the stator radius.

Looking at these equations reveals that the bearing forces and the motor torque can be derived with the knowledge of the flux density in the air gap and the current density distribution on the stator surface, whereby the flux density in the air gap is the superposition of the flux density of the permanent magnets (PMs) and the flux density that is caused by the stator windings. As can be seen in (6) and (7), the resulting bearing force and the torque are both depending on the rotor angle. Strictly speaking, the magnitudes obtained in (6) and (7) are acting on the stator. Thus, the respective forces $\mathbf{F}_r$ and torque M_r acting on the rotor are calculated with

$$\mathbf{F}_r = -\,\mathbf{F}_s \tag{8}$$

$$M_r = -\,M_s. \tag{9}$$

Before this model can provide the basis for the analysis of the different concepts, simulations of all the topologies must be carried out in order to identify the electromagnetic field distribution in the different motor embodiments. Although analytical equations may serve in some cases for the estimation of the flux density in the air gap, an accurate calculation should be based on 2-D or 3-D finite-element-method simulation results. In the presented case in this paper, the simulations are carried out with the simulation program Maxwell [14]. Given a specific load point in a pump application with the therein required torque on the impeller and the arising bearing forces to stabilize it, the currents in the drive and bearing system can be obtained with this mathematical model. These currents provide the basis for the copper and semiconductor loss comparison of the different motor configurations. Furthermore, the electromagnetic field distribution obtained by simulations also provides the base for the evaluation of the eddy current and hysteresis losses in the iron circuit of the respective motor embodiments. The calculations and simulation results are shown in Section IV.

III. Investigated BSM Configurations

With regard to the previously discussed performance indexes, different BSM configurations suitable for pump applications in general are assessed in the following. The targeted pump applications are specified by the maximum rotational speed, the rated torque, and the maximum bearing force. As a base for the comparison, the following assumptions are considered for the design of the BSM.

1) The required rated drive power at the chosen operating point is $P_{\mathrm{DR}} = 1200$ W.
2) The bearing system is designed in order to ensure sufficient levitation forces for the whole operating range.
3) The rotor diameter and the stator bore, respectively, are the same for all the chosen configurations.
4) At rated torque, the current density in the drive windings is the same for all the chosen configurations.
5) The flux density in the iron circuit is assumed to be the same for motor configurations (a)–(d). Furthermore, these configurations are realized as a temple motor, whereas configuration (e) is a disk-shape configuration.

With these assumptions, the assessment of the bearingless motors shown in Fig. 4 has been carried out. The configurations are the following.

1) Fig. 4(a) shows a two-phase BSM with 12 separate windings for the drive and bearing system and a two-pole (pole pair number $p = 1$) PM rotor. This symmetrical winding configuration represents the standard setup in today's

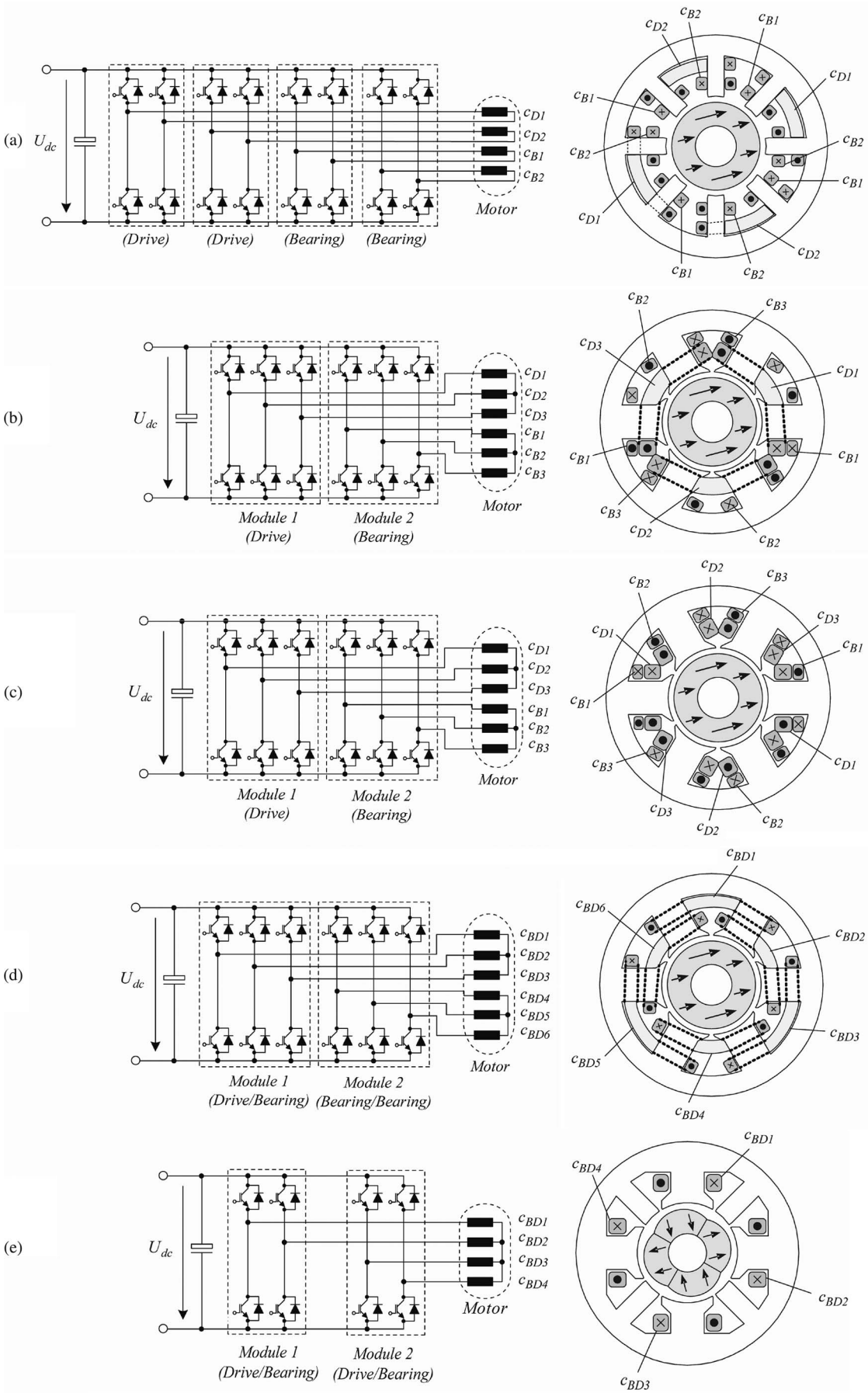

Fig. 4. Investigated BSM systems (a)–(e) consisting of the converter and the corresponding motor configuration.

bearingless pump systems [15] and possesses a total of eight claws. In order to independently generate the levitation forces and the motor torque, eight full bridges are needed, consisting of a total of 16 power transistors. However, as has been shown in recent research [16], this motor embodiment could also be operated with only six half bridges. In order to ensure full control flexibility, special modulation schemes must be employed [17]. For the comparison in this paper, the standard full-bridge configuration will be used for the sake of fair comparability with the other concepts.

2) Fig. 4(b) shows a three-phase BSM with six claws and nine separate windings for the drive and bearing systems and a two-pole $(p = 1)$ PM rotor. In contrast to motor configuration (a), the currents in the drive windings do not only generate the motor torque but also cause shear forces which then need to be compensated by the bearing currents and thus possibly lead to higher losses. This drawback can be overcome with an adequate control algorithm. With this, the currents applied to the drive windings only lead to the generation of the desired torque without influencing the stable levitation of the impeller. The subsequent calculation of the copper losses for this motor embodiment is carried out with regard to this optimized control scheme.
3) Fig. 4(c) shows a three-phase BSM with six claws and 12 separate windings forming the drive and bearing systems and a two-pole $(p = 1)$ PM rotor. In this configuration, the drive currents do not lead to a generation of bearing forces as it is the case for the previously described configuration.
4) Fig. 4(d) is an interesting novel three-phase BSM topology with six claws and six coils which generate the torque and the axial forces in common. The current rating is the same for all coils, and again, a two-pole $(p = 1)$ PM rotor is employed. The pitch winding configuration results in a more efficient torque generation and lower power losses compared with those of the motor embodiments (a)–(c) as will be shown later on.
5) Fig. 4(e) shows a four-phase BSM with four concentrated coils and a four-pole $(p = 2)$ PM rotor. Contrary to the previously described configurations, which are realized in a temple motor design with each claw being placed in an orthogonal manner to the back iron, this motor is preferably realized in a disk shape with a homogeneously oriented lamination of the iron sheets. The absence of intersections between the claws and the back iron in this configuration has a major impact on the total iron loss reduction as will be shown later on. Although the motor has four phases, the torque generation has a single-phase motor characteristic. Furthermore, it offers the benefit that only four power half bridges are needed to generate the torque and levitation currents in the motor.

The advantage of the converter topologies (b), (c), and (d) is that three-phase power modules with integrated features such as gate drivers and overcurrent detection can be applied, which leads to a significantly higher compactness. Furthermore, the manufacturing cost is lowered, since such power modules are used in a large variety of applications and thus produced in high numbers.

As an immanent property of the motor embodiments shown in Fig. 4(d) and (e), the rated currents of all windings are showing the same value, which leads to a good utilization of the power electronics. On the other hand, the concentrated coils contribute to a coupled and highly nonlinear force and torque generation and thus require a more complex control algorithm in order to safely operate the motor. Contrary, for the configurations shown in Fig. 4(a)–(c), separate winding systems for force and torque generation are used. This results in different current ratings for the drive and bearing windings and hence leads to an unbalanced utilization of the semiconductor devices if identical three-phase power modules are utilized. In order to quantify these facts, a detailed comparison will be carried out in the following.

IV. Loss Calculation

The evaluation of the losses in the motor and the power electronics is indispensable for a thorough comparison of the motor concepts. The most important portion is the copper losses occurring in the windings of the motor. In order to obtain a better comparability between motors (a)–(e), the same current densities in the drive and bearing windings, respectively, have been assumed as design criteria for the calculation of the windings. A further important portion is the speed-dependent iron losses, which are evaluated for all the presented embodiments subsequently. In Section IV-C, the equations for the calculation of the switching and forward losses occurring in the power semiconductors are presented. With this, the total losses will be comparatively evaluated for the five concepts.

A. Copper Losses

The calculation of the copper losses in the motor phases is given by the following:

$$P_{\mathrm{Cu}} = \sum_{i=1}^{m} R_i \cdot I_{i,\mathrm{rms}}^2 \tag{10}$$

where m is the number of winding phases of the subjected motor and R_i is the corresponding resistance value, which is calculated with

$$R_i = \frac{\rho_{\mathrm{Cu}} \cdot l_w}{A_{\mathrm{Cu}}}. \tag{11}$$

Here, l_w stands for the average winding length of the drive or bearing winding, ρ_{Cu} is the specific resistance of copper, and A_{Cu} is the wire cross area. Due to the concentrated coils and the chosen design of the motor configurations, there exist no end windings that must be included in the calculation of the copper losses.

Doing this for all of the motor embodiments shown in Fig. 4 for the load point specified in Section III leads to a loss distribution as shown in Fig. 5. Looking at the values at zero bearing force reveals that motor embodiment (d) only generates 56% of the losses occurring in configuration (b). While increasing the bearing force up to 100% (which equals 20 N), this proportion

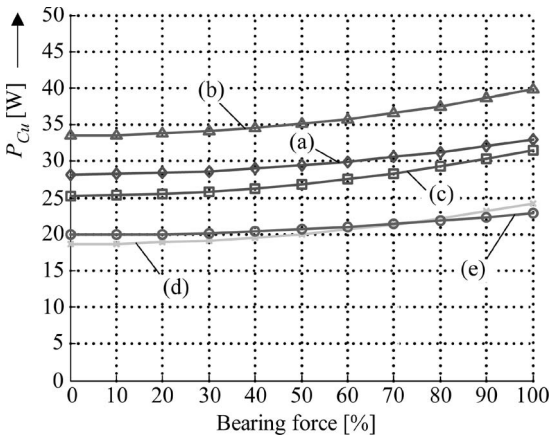

Fig. 5. Total copper losses subject to an increasing levitation force at the design point of a 1200-W drive power for the motor configurations (a)–(e) shown in Fig. 4. 100% equals the maximum bearing force requested in a transient condition.

stays almost the same. The largest increase in losses due to the generation of the levitation forces arises for motor (d). Therefore, at maximum force, the losses are increased by 30% compared to the load point with no currents in the bearing phases.

B. Iron Losses

According to [18], the hysteresis losses of iron can be approximated under the assumption that the magnitude of the flux density $\hat{B}$ of an alternating field is in the range of 0.2–1.5 T by the following:

$$P_{\mathrm{Hy}} = c_{\mathrm{Hy}} \cdot f_e \cdot \hat{B}^{1.6} \cdot m_{\mathrm{Fe}}. \tag{12}$$

The hysteresis losses are thus linearly dependent on a material constant c_{Hy}, the electrical frequency f_e of the motor, and the iron mass m_{Fe}, while the dependence on the flux density is of higher order. On the other hand, the eddy current losses [19] in the stator iron are given by

$$P_{\mathrm{Ed}} = c_{\mathrm{Ed}} \cdot f_e^2 \cdot \hat{B}^2 \cdot d_{\mathrm{Fe}}^2 \cdot m_{\mathrm{Fe}} \tag{13}$$

if the iron circuit is built up with isolated laminated sheets with a thickness of d_{Fe}.

However, for the evaluation of the hysteresis and eddy current losses, the magnetic flux density in the iron path cannot be assumed to have a homogeneous distribution; wherefore, (12) and (13) cannot be used directly. In Fig. 6, this circumstance is illustrated by the field distribution in the iron circuit of the polyphase motor configuration shown in Fig. 4(e).

In order to calculate the iron losses accurately, the whole stator needs to be segmented into k parts with each having a constant flux density $\hat{B}_i$ and a mass $m_{\mathrm{Fe},i}$. The whole iron losses of each motor configuration can then be calculated according to

$$\begin{aligned} P_{\mathrm{Fe}} &= P_{\mathrm{Hy}} + P_{\mathrm{Ed}} \\ &= m_{\mathrm{Fe},i} \cdot \left(c_{\mathrm{Hy}} \cdot f_e \cdot \sum_i^k \hat{B}_i^{1.6} + c_{\mathrm{Ed}} \cdot f_e^2 \cdot \sum_i^k \hat{B}_i^2 \cdot d_{\mathrm{Fe}}^2 \right). \end{aligned} \tag{14}$$

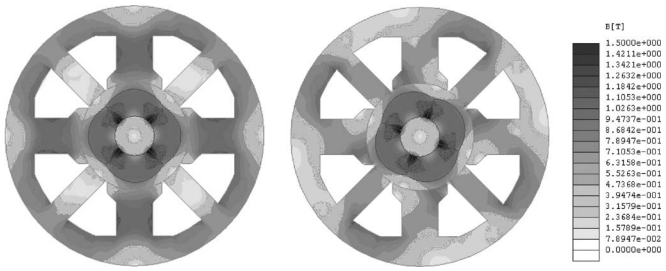

Fig. 6. Flux density distribution in the iron circuit of motor embodiment (e) (cf. Fig. 4) caused by the PM for rotor angles of 0° and 25°.

TABLE I
IRON LOSS FACTORS

Configuration	(a)	(b),(c),(d)	(e)
k_1 [W/1000 rpm]	0.921	0.850	0.671
k_2 [W/(1000 rpm)^2]	0.645	0.602	0.153

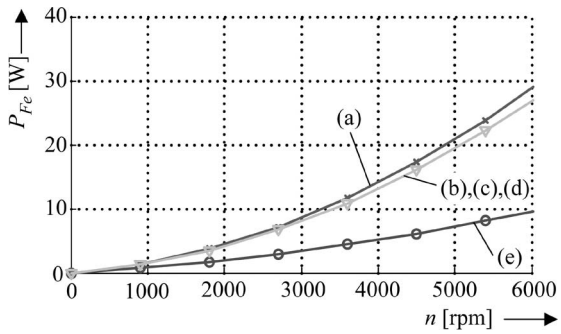

Fig. 7. Total iron losses P_{Fe} of the presented motor configurations (a)–(e) depending on the motor speed n.

This correlation can also be written as

$$P_{\mathrm{Fe}} = k_1 \cdot n_e + k_2 \cdot n_e^2 \tag{15}$$

where k_1 is the linear loss factor, k_2 is the square loss factor, and n is the motor speed. These factors, which have been extracted from simulations and validated by measurements on experimental test setups, are compiled in Table I for all configurations.

It can be seen that, particularly, the square loss factor (due to the eddy current losses) is significantly lower for configuration (e). The main reason is the fully radial construction of that setup with an equally oriented lamination of the iron sheets. Contrary, the concepts (a)–(d) are built in a temple motor design, where the stator parts have to be linked in an orthogonal manner and a continuous lamination is not possible. Furthermore, setup (e) has a lower iron mass, which is, however, compensated by the higher electrical frequency (due to $p = 2$).

In total, as shown in Fig. 7, a clear advantage for the motor configuration (e) is given regarding the iron losses, particularly for higher rotational speeds. However, due to dynamical limitations (as will be discussed later), this concept does not allow rotational speeds above 8000 r/min, which is a limiting factor for some applications.

C. Power Electronic Losses

All of the presented motor configurations are operated with a symmetrical pulsewidth modulation switching pattern. Due to this and the utilization of similar components in the drive and bearing system of all configurations, the switching losses can be evaluated based on the same switching loss energy data. The switching losses of a device are then given by the integration of the loss energy over a $\pi/2$-wide interval

$$P_{\mathrm{Sw}} = f_s \cdot \frac{2}{\pi} \int_0^{\pi/2} w(i) d\varphi. \tag{16}$$

With the assumption of a linear dependence of the loss energy on the switched current

$$w(i) = k_i \cdot i \tag{17}$$

for a given voltage, the calculation of the switching losses based on the component specific factors k_{on}, k_{off}, and k_{rev} for the turn-on, the turn-off, and the reverse recovery losses, respectively, can be utilized. These parameters, which have been evaluated by switching loss measurements on a three-phase power module [20], account to $k_{\mathrm{on}} = 22.54\ \mu$J/A, $k_{\mathrm{off}} = 11.43\ \mu$J/A, and $k_{\mathrm{rev}} = 1.35\ \mu$J/A for a dc-link voltage of $U_{\mathrm{dc}} = 325$ V. For the sake of a fair comparison, these parameters have also been used for the full-bridge topology (cf. Fig. 4(a), two-phase configuration) and the half-bridge topology (cf. Fig. 4(e), four-phase configuration). With this, the total switching losses per bridge leg are given by

$$P_{\mathrm{PE,Sw}} = \frac{2 \cdot f_s}{\pi} \cdot (k_{\mathrm{on}} + k_{\mathrm{off}} + k_{\mathrm{rr}}) \cdot \hat{I}. \tag{18}$$

The forward characteristics of the semiconductors can be approximated by a forward voltage drop and a forward resistance. The parameters $U_{\mathrm{CE},0}$ and r_{CE} for the insulated-gate bipolar transistor and $U_{F,0}$ and r_F for the diode, respectively, have also been evaluated by measurements and account to $U_{\mathrm{CE},0} = 1.11$ V, $r_{\mathrm{CE}} = 77$ mΩ, $U_{F,0} = 1.05$ V, and $r_F = 83$ mΩ. With this, the conduction losses of any semiconductor can be derived by

$$P_{\mathrm{Fw},T} = U_{\mathrm{CE},0} \cdot I_{T,\mathrm{avg}} + r_{\mathrm{CE,on}} \cdot I^2_{T,\mathrm{rms}} \tag{19}$$

$$P_{\mathrm{Fw},D} = U_{F,0} \cdot I_{D,\mathrm{avg}} + r_F \cdot I^2_{D,\mathrm{rms}}. \tag{20}$$

The total power electronic losses in the half bridges due to the bearing and drive currents can then be evaluated.

D. Total Losses

With the help of the aforementioned equations, the overall losses P_L including the copper, the iron, and the power electronic losses can be calculated. Their distribution is shown in Fig. 8.

This comparison has been carried out for a rated drive power of $P_{\mathrm{DR}} = 1200$ W at 70% bearing force at a speed of $n = 3600$ r/min, which is a typical operating point value. It can be seen that the total losses are lowest for configuration (e), followed by setup (d).

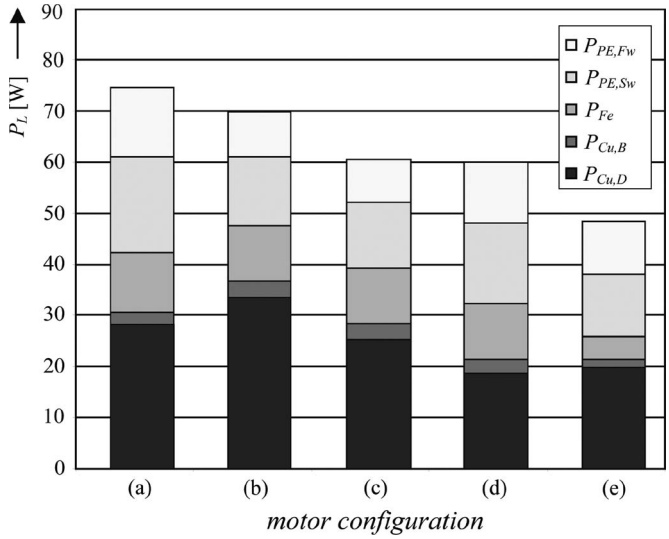

Fig. 8. Overall loss distribution for the motor and converter configurations shown in Fig. 4(a)–(e). The shown losses are the copper losses in the drive system ($P_{\mathrm{Cu},D}$) and in the bearing system ($P_{\mathrm{Cu},B}$), the iron losses (P_{Fe}), the switching losses ($P_{\mathrm{PE,Sw}}$), and the forward losses ($P_{\mathrm{PE,Fw}}$) in the power electronics.

V. Power Electronic Requirements

Another important figure for the evaluation of the motor topologies is their VA power electronic requirement. In the past, a lot of research has been carried out on the VA requirements of different motors [21], [22]. Among different definitions, the VA rating in terms of the inverter peak voltage and rms current of the motor is the most suitable for the comparison of the evaluated BSM topologies.

The VA rating in a mathematical form is given by

$$P_{\mathrm{VA}} = \sum_{i=1}^{m} \hat{U}_i \cdot I_{i,\mathrm{rms}} \tag{21}$$

with the rms current $I_{i,\mathrm{rms}}$ and the peak phase voltage $\hat{U}_i$. When neglecting the resistive voltage drop across the drive or bearing winding, the required value of the peak phase voltage $\hat{U}_i$ results in

$$\hat{U}_i = \sqrt{(\omega L_i \hat{I}_i)^2 + \hat{U}^2_{i,\mathrm{ind}}} \tag{22}$$

with the phase inductance L_i, the peak phase current $\hat{I}_i$, and the amplitude of the induced voltage $\hat{U}_{i,\mathrm{ind}}$.

For the configurations (a)–(c), which feature separated drive and bearing systems, different peak phase voltage requirements can be calculated for both systems. However, due to the availability of only one common dc-link voltage of the converter, the higher voltage requirement (which occurs for the drive system) has been considered for both systems. Hence, the bearing system has a broad stability margin to compensate for external disturbances. For the configurations (d)–(e), which generate the levitation forces and the torque in the same windings, a certain stability margin for the bearing system has to be added explicitly in order to also guarantee a safe operation. Measurements on laboratory prototypes have shown that the voltage requirement has to be increased by a factor of 1.3 for

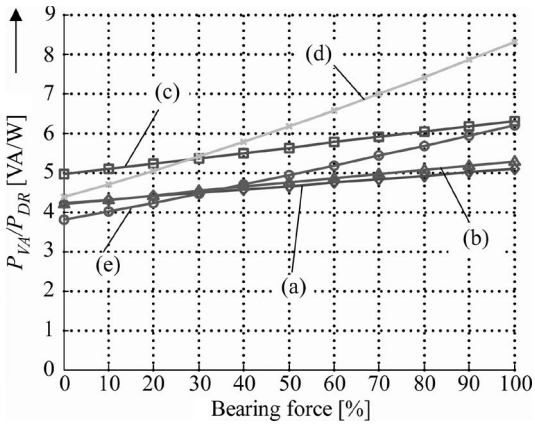

Fig. 9. Normalized VA requirement of the presented motor configurations (normalization basis is rated drive power $P_{\mathrm{DR}} = 1200$ W).

the considered speed range, which is already taken into account for this comparative evaluation. For higher rotational speeds, this margin would have to be increased even more, and it was observed experimentally that, for a dc-link voltage of 325 V, the configurations (d) and (e) can no longer be operated above 8000 r/min. Additionally, for configuration (e), the maximum achievable speed is also limited by the digital control, which has to deal twice the electrical frequency due to $p = 2$ as compared with the other topologies.

The VA requirements scaled to the rated mechanical power are shown in Fig. 9 for the different motor designs. One can see that the required bearing forces have significant impact on the VA requirement of the motor. This is particularly the case for motor (d), where, at 100% bearing force, which equals 20 N, the VA requirement is nearly doubled as compared to zero force. If only the drive system is taken into account (0% bearing force), configuration (e) demands the lowest VA requirement.

However, this condition does not arise in normal operations of a BSM since levitation forces are always needed in order to safely operate the system. For the considered operating point with 70% bearing forces, which is a typical value for pump applications, motor configurations (a) and (b) are the most efficient solutions regarding the necessary VA requirement of the converter.

VI. Overall Performance Comparison

As mentioned in the beginning, BSM pump systems are getting more and more targeted for applications, where mass production becomes feasible. Therefore, additional cost-related factors must be taken into consideration for a complete comparison. In Table II, a qualitative comparison of the concepts is given for these factors in addition to the previously discussed performance indexes (power losses and VA requirement).

As has been shown in Section IV, configurations (d) and (e) are the favorable ones, if only the losses in the motor and the power electronics are considered. At the chosen operating point, the overall losses occurring in configuration (e) are 65% of those resulting in configuration (a).

In terms of VA requirements, the motor setups (a) and (b) have been found to be preferable for applications where significant bearing forces occur, e.g., for pumps. On the other hand, configuration (d) has the highest VA requirements and therefore leads to the largest power electronic volume.

TABLE II
Qualitative Comparison of the Different BSM Concepts

Motor	(a)	(b)	(c)	(d)	(e)
Power losses	–	–	✓	✓	+
VA requirement	+	+	✓	–	✓
Copper/Iron mass	–	–	–	–	+
Realisation effort	✓	✓	✓	✓	+
Control complexity	+	+	+	–	–
Scalability	+	+	+	–	–

The comparison of the copper and iron masses, which is required to realize the different motor embodiments, is lowest for configuration (e). The radial design of the iron circuit, which does not need additional vertical claws, as they are required in the temple motor configurations (a)–(d), results in an iron mass which is almost half as compared with the other concepts.

Looking at the embodiments from a manufacturing perspective and considering the necessary realization effort reveals motor (e) as the most promising solution. This mainly emerges from the disk-shape structure of this configuration, which offers certain production advantages. First, the four identical coils can be directly wound on the stator claws in one step, which simplifies the manufacturability. In addition, the iron circuit can be realized with a horizontally laminated iron stack. Due to the absence of additional vertical claws, the manufacturing effort is clearly reduced compared with the temple motor configurations (a)–(d). Finally, the disk-shape setup also offers the possibility of integrating the power electronic part in the motor while still keeping the thereby resulting total case volume in the range of the temple motor configurations without integrated power electronics. In addition, this greatly reduces the cabling effort. However, the sensor concept of motor (e) for the position detection of the impeller is the most difficult of all the presented configurations due to the shape of the iron circuit and the limited space that is available for the insertion of the sensors. Its design also influences the design of the pump impeller in terms of hydraulic efficiency. This fact also strongly influences the applicability of this concept in high-pressure/flow applications. However, taking all the aforementioned issues into account, the realization effort is clearly the lowest for configuration (e).

The control complexity of the presented motor embodiments highly depends on the chosen winding configuration. The fact that the currents, which are generating torque and levitation forces, are applied to the same coils common for configurations (d) and (e) results in a more sophisticated control structure as it is the case for configurations (a)–(c). In the latter, the control of the drive and bearing system can be done independently. This results in a less complex control structure as for motors (d) and (e).

As explained in Section V, the scalability of the motor configurations toward higher speeds and pressure is best for configurations (a)–(c). This results from the independent drive and bearing system, where, due to the utilization of the same dc-link voltage, the bearing system usually features a large dynamical voltage margin to compensate for external disturbances.

In contrast, for configurations (d) and (e), the stability margin for the bearing system has to be added explicitly in order to guarantee a safe operation. This voltage margin, together with the maximum available dc-link voltage, is the limiting factor for the maximum achievable drive speed for these concepts. In today's semiconductor applications, a strong demand arises for pumps with high-pressure ratings. For these applications, motor configurations (d) and (e) cannot be considered as suitable solutions due to their limited speed capability.

Summing up, it can be stated that configuration (e) is highly interesting for future cost-sensitive bearingless motor applications such as pumps for the plating industry, mixers for biotechnology processes, or heat and cooling pumps. However, the applicability of this configuration is limited to the low/medium speed range and is therefore not suitable for high-pressure applications. In this area, configuration (a) still seems to be the most preferable solution.

VII. Conclusion

In this paper, two-, three-, and four-phase BSMs have been comparatively discussed based on performance indexes in order to find the most suitable motor embodiment for more cost-sensitive application areas of next-generation bearingless pump systems. The comparison has been carried out for a typical pump operating point (rated mechanical drive power of 1200 W and bearing forces in the range of 0–20 N), and the performance indexes have been defined as the occurring power losses in the converter and the motor, the power electronic VA requirements in order to achieve the operating point, and the cost-related manufacturing issues (such as copper and iron masses, realization effort in consideration of mass production, control complexity, and scalability toward higher speed and pressure ranges).

The comparison has not revealed a clear superior concept in all aspects, but has given a better insight to the specific attributes and possibilities of each concept. Generally, it can be stated that the three-phase motor configurations (b)–(d) do not show a clear advantage in none of the considered aspects; wherefore, they will barely be selected as the next-generation bearingless motor concept.

On the other hand, the four-phase motor configuration (e) seems to be a promising concept for future cost-sensitive applications in the low pressure range and low/medium speed range, e.g., pumps for the plating industry, mixers for biotechnology processes, or heat and cooling pumps. The advantages of this concept in terms of small iron and copper masses and easy manufacturability are mainly arising from its radial construction. In addition, the compact design allows the integration of the power electronics in the motor housing with a resulting volume comparable to that of the temple motor design without integrated electronics.

However, for high-pressure applications in upcoming semiconductor applications, where speeds above 8000 r/min are demanded, this concept can no longer be considered due to its inherent speed limitations. Therefore, the standard two-phase topology (a) is still the most preferable solution due to the independent drive and bearing winding system.

References

[1] M. Neff, N. Barletta, and R. Schöb, "Magnetically levitated centrifugal pump for highly pure and aggressive chemicals," in *Proc. PCIM Conf.*, Nuremberg, Germany, Jun. 6–8, 2000.

[2] R. Schöb, N. Barletta, and J. Hahn, "The bearingless centrifugal pump—A perfect example of a mechatronics system," in *Proc. 1st IFAC Conf. Mechatronic Syst.*, Darmstadt, Germany, Sep. 18–20, 2000.

[3] A. Chiba, R. Furuichi, Y. Aikawa, K. Shimada, Y. Takamoto, and T. Fukao, "Stable operation of induction-type bearingless motors under loaded conditions," *IEEE Trans. Ind. Appl.*, vol. 33, no. 4, pp. 919–924, Jul./Aug. 1997.

[4] M. Ohsawa, S. Mori, and T. Satoh, "Study of the induction type bearingless motor," in *Proc. 7th Int. Symp. Magn. Bearings*, Zurich, Switzerland, Aug. 2000, pp. 389–394.

[5] A. Chiba, T. Deido, T. Fukao, and M. A. Rahman, "An analysis of bearingless AC motors," *IEEE Trans. Energy Convers.*, vol. 9, no. 1, pp. 61–67, Mar. 1994.

[6] M. Neff, N. Barletta, and R. Schöb, "Bearingless centrifugal pump for highly pure chemicals," in *Proc. 8th Int. Symp. Magn. Bearings*, Mito, Japan, Aug. 2002, pp. 283–287.

[7] W. K. S. Khoo, R. L. Fittro, and S. D. Garvey, "AC polyphase self-bearing motors with a bridge configured winding," in *Proc. 8th Int. Symp. Magn. Bearings*, Mito, Japan, Aug. 2002, pp. 47–52.

[8] Y. Okada, K. Dejima, and T. Ohishi, "Analysis and comparison of PM synchronous motor and induction motor type magnetic bearings," *IEEE Trans. Ind. Appl.*, vol. 31, no. 5, pp. 1047–1053, Sep./Oct. 1995.

[9] Y. Okada, S. Miyamoto, and T. Ohishi, "Levitation and torque control of internal permanent magnet type bearingless motor," *IEEE Trans. Control Syst. Technol.*, vol. 4, no. 5, pp. 565–571, Sep. 1996.

[10] N. Barletta and R. Schöb, "Design of a bearingless blood pump," in *Proc. 3rd Int. Symp. Magn. Suspension Technol.*, Tallahassee, FL, 1995, pp. 265–274.

[11] S. Silber, W. Amrhein, P. Bosch, R. Schöb, and N. Barletta, "Design aspects of bearingless slice motors," *IEEE/ASME Trans. Mechatronics*, vol. 10, no. 6, pp. 611–617, Dec. 2005.

[12] D. Schröder, *Elektrische Antriebe—Grundlagen*., 2nd ed. New York: Springer-Verlag, 2000.

[13] K. Simonyi, *Theoretische Elektrotechnik*. Leipzig, Germany: Barth Verlagsgesellschaft GmbH, 1993.

[14] Maxwell 3D distributed by Ansoft Corporation. [Online]. Available: http://www.ansoft.com

[15] Levitronix Pumps. [Online]. Available: http://www.levitronix.com

[16] M. T. Bartholet, T. Nussbaumer, P. Dirnberger, and J. W. Kolar, "Novel converter concept for bearingless slice motor systems," in *Conf. Rec. 41st IEEE IAS Annu. Meeting*, Tampa, FL, Oct. 2006, vol. 5, pp. 2496–2502.

[17] M. T. Bartholet, T. Nussbaumer, D. Krähenbühl, F. Zürcher, and J. W. Kolar, "Modulation concepts for the control of a two-phase bearingless slice motor utilizing three-phase power modules," in *Proc. IEEE Power Convers. Conf.*, Nagoya, Japan, 2007, pp. 816–823.

[18] C. P. Steinmetz, "On the law of hysteresis," *Proc. IEEE*, vol. 72, no. 2, pp. 196–221, Feb. 1984.

[19] C. Heck, *Magnetische Werkstoffe und ihre technische Anwendung*. Heidelberg, Germany: Dr. Alfred Hüthig, 1975. 2. Auflage.

[20] International Rectifier, Integrated Power Hybrid IC for Appliance Motor Drive Applications, IRAM136-3063B, Preliminary Datasheet DR-2, El Segundo, CA, 2007.

[21] M. Barnes and C. Pollock, "Power electronic converters for switched reluctance drives," *IEEE Trans. Power Electron.*, vol. 13, no. 6, pp. 1100–1111, Nov. 1998.

[22] T. J. E. Miller, *Switched Reluctance Motors and Their Control*. Oxford, U.K.: Magna Physics, 1993.

Martin T. Bartholet (M'09) received the B.S. degree in electrical engineering, dealing with power electronics, machines, and magnetic bearings, and the M.Sc. and Ph.D. degrees in 2004 and 2008, respectively, from the Swiss Federal Institute of Technology (ETH) Zurich, Zurich, Switzerland, where he performed research on magnetically levitated motors and pumps for the semiconductor industry during his Ph.D. studies.

At Chalmers University of Technology, Göteborg, Sweden, he worked with wind turbines. Since August 2008, he has been with Celeroton AG, Zurich, Switzerland, where he is working on ultra-high-speed electric drive systems.

Thomas Nussbaumer (S'02–M'06) was born in Vienna, Austria, in 1975. He received the M.Sc. degree (with honors) in electrical engineering from the University of Technology Vienna, Vienna, Austria, in 2001, and the Ph.D. degree from the Power Electronic Systems (PES) Laboratory, Swiss Federal Institute of Technology (ETH) Zürich, Zürich, Switzerland, in 2004.

From 2001 to 2006, he was with the PES, where he conducted research on modeling, design, and control of three-phase rectifiers, power factor correction techniques, and electromagnetic compatibility. Since 2006, he has been with Levitronix GmbH, Zürich, Switzerland, where he is currently working on bearingless motors, magnetic levitation, and permanent-magnet motor drives for the semiconductor and biotechnology industry. His current research is focused on compact and high-performance mechatronic systems including novel power electronics topologies, control techniques, drive systems, sensor technologies, electromagnetic interference (EMI), and thermal aspects.

Siegfried Silber (S'95–A'99–M'03) received the Dipl.Ing. degree in electrical engineering from Graz University of Technology, Graz, Austria, in 1995, and the Ph.D. degree from Johannes Kepler University Linz, Linz, Austria, in 2000.

Since 2000, he has been a Senior Researcher at Johannes Kepler University Linz and the Linz Center of Mechatronics GmbH, where he has been involved in research projects. His research interests include magnetic bearings, bearingless motors, brushless motors, and power electronics.

Johann W. Kolar (M'89–SM'04) received the Ph.D. degree (*summa cum laude/promotio sub auspiciis praesidentis rei publicae*) from the University of Technology Vienna, Austria.

Since 1984, he has been an Independent International Consultant in close collaboration with the Vienna University of Technology, in the fields of power electronics, industrial electronics, and high-performance drives. On February 1, 2001, he was appointed as a Professor and Head of the Power Electronic Systems Laboratory, Swiss Federal Institute of Technology (ETH), Zürich, Switzerland. He has proposed numerous novel PWM converter topologies, and modulation and control concepts, e.g., the VIENNA rectifier and the three-phase ac–ac sparse matrix converter. He has published over 300 scientific papers in international journals and conference proceedings. He is the holder of 75 patents. His current research is on ac–ac and ac–dc converter topologies with low effects on the mains, e.g., for power supply of telecommunication systems, more electric aircraft, and distributed power systems in connection with fuel cells. His other main areas of research include the realization of ultracompact intelligent converter modules employing latest power semiconductor technology (SiC), novel concepts for cooling and EMI filtering, multidomain/multiscale modeling and simulation, pulsed power, bearingless motors, and power MEMS.

Dr. Kolar is a member of the Institute of Electrical Engineers of Japan (IEEJ) and the technical program committees of numerous international conferences in the field (e.g., Director of the Power Quality Branch of the International Conference on Power Conversion and Intelligent Motion). From 1997 to 2000, he served as an Associate Editor of the IEEE TRANSACTIONS ON INDUSTRIAL ELECTRONICS, and since 2001, as an Associate Editor of the IEEE TRANSACTIONS ON POWER ELECTRONICS. Since 2002, he has been an Associate Editor for the *Journal of Power Electronics* of the Korean Institute of Power Electronics and a member of the Editorial Advisory Board of the *IEEJ Transactions on Electrical and Electronic Engineering*. He was the recipient of the Best Transactions Paper Award of the IEEE Industrial Electronics Society in 2005 and an Erskine Fellowship from the University of Canterbury, New Zealand, in 2003. In 2006, the European Power Supplies Manufacturers Association awarded the Power Electronics Systems Laboratory of ETH Zürich as the leading academic research institution in Europe.